

A COMPARISON OF TWO- AND THREE-DIMENSIONAL NEUTRINO-HYDRODYNAMICS SIMULATIONS OF CORE-COLLAPSE SUPERNOVAE

TOMOYA TAKIWAKI¹, KEI KOTAKE^{2,1}, AND YUDAI SUWA³

¹Center for Computational Astrophysics, National Astronomical Observatory of Japan, 2-21-1, Osawa, Mitaka, Tokyo, 181-8588, Japan

²Department of Applied Physics, Fukuoka University, Fukuoka 814-0180, Japan and

³Yukawa Institute for Theoretical Physics, Kyoto University, Oiwake-cho, Kitashirakawa, Sakyo-ku, Kyoto, 606-8502, Japan
for ApJ

ABSTRACT

We present numerical results on two- (2D) and three-dimensional (3D) hydrodynamic core-collapse simulations of an $11.2M_{\odot}$ star. By changing numerical resolutions and seed perturbations systematically, we study how the postbounce dynamics is different in 2D and 3D. The calculations were performed with an energy-dependent treatment of the neutrino transport based on the isotropic diffusion source approximation scheme, which we have updated to achieve a very high computational efficiency. All the computed models in this work including nine 3D models and fifteen 2D models exhibit the revival of the stalled bounce shock, leading to the possibility of explosion. All of them are driven by the neutrino-heating mechanism, which is fostered by neutrino-driven convection and the standing-accretion-shock instability (SASI). Reflecting the stochastic nature of multi-dimensional (multi-D) neutrino-driven explosions, the blast morphology changes from models to models. However, we find that the final fate of the multi-D models whether an explosion is obtained or not, is little affected by the explosion stochasticity. In agreement with some previous studies, higher numerical resolutions lead to slower onset of the shock revival in both 3D and 2D. Based on the self-consistent supernova models leading to the possibility of explosions, our results systematically show that the revived shock expands more energetically in 2D than in 3D.

Subject headings: supernovae: general — neutrinos — hydrodynamics

1. INTRODUCTION

Ever since the first numerical simulation of core-collapse supernovae (CCSNe) (Colgate & White 1966), the neutrino-driven mechanism has been the leading candidate of the explosion mechanism for more than four decades. In the long history, a very important lesson we have learned from Rampp & Janka (2000); Liebendörfer et al. (2001); Thompson et al. (2003); Sumiyoshi et al. (2005) near the Millennium, is that the spherically-symmetric (1D) form of this mechanism fails to explode canonical massive stars. Supported by accumulating supernova observations of the blast morphology (e.g., Wang & Wheeler (2008), and references therein), a number of multi-dimensional (multi-D) hydrodynamic simulations have been reported so far, which gives us a confidence that hydrodynamic motions associated with neutrino-driven convection (e.g., Herant et al. (1994); Burrows et al. (1995); Janka & Müller (1996); Fryer et al. (2002) and see collective references in Burrows et al. (2012); Murphy et al. (2013); Couch (2013)) and the SASI (e.g., Blondin et al. (2003); Scheck et al. (2004, 2006); Ohnishi et al. (2006, 2007); Ott et al. (2008); Murphy & Burrows (2008); Foglizzo et al. (2006, 2007, 2012); Iwakami et al. (2008, 2009, 2013); Endeve et al. (2010, 2012); Fernández & Thompson (2009a,b); Fernández (2010); Hanke et al. (2012)) can help the onset of neutrino-driven explosions.

In fact, a growing number of neutrino-driven explosions have been recently obtained in the state-of-the-art two-dimensional (2D) simulations, in which spectral neutrino transport is solved with different levels of sophistication (e.g., Buras et al. (2006); Marek & Janka

(2009); Müller et al. (2012, 2013); Bruenn et al. (2013); Suwa et al. (2010, 2011, 2013), Janka (2012) for a review). This success is, however, accompanying new questions. Among them¹, three-dimensional (3D) effects on the neutrino-driven mechanism are attracting a paramount attention (e.g., Burrows (2013); Kotake et al. (2012) for a review). Unfortunately, however, experimental 3D models that employed a light-bulb scheme (e.g., Murphy & Burrows (2008)), have provided divergent results so far. The basic result of Nordhaus et al. (2010) who were the first to point out that 3D leads to easier explosions than 2D, has been supported by the follow-up studies (Burrows et al. 2012; Dolence et al. 2013), but not by Hanke et al. (2012); Couch (2013). On top of the urgent task to make a detailed comparison between these idealized models, self-consistent 3D simulations should be done in order to have the final word on the 3D effects.

At present, 3D CCSN simulations including spectral neutrino transport are only few (Hanke et al. 2013; Takiwaki et al. 2012). Very recently, Hanke et al. (2013) succeeded in performing 3D simulations with detailed neutrino transport for a $27 M_{\odot}$ star. In addition to the first discovery regarding the violent SASI activity in self-consistent 3D models, their results illuminate the importance to go beyond the prevalent light-bulb scheme, only by doing so, the non-linear couplings such as between core-contraction of the proto-neutron star (PNS), the accretion neutrino luminosity, and the multi-D hydrodynamic feedback of neutrino-driven convection and

¹ Note that general relativity (GR, e.g., Müller et al. (2012); Kuroda et al. (2012); Ott et al. (2013)) and detailed weak interactions (e.g., Langanke et al. (2008); Furusawa et al. (2013)) are considered as important as 3D effects.

the SASI, can be self-consistently determined. On the other hand, the very high computational cost allowed Hanke et al. (2013) to focus on a single (self-consistent) 3D model, and it has not been clarified yet whether 3D helps or harms the onset of neutrino-driven explosions compared to 2D.

To address this question, we investigate in this paper how the explosion dynamics will differ from 3D to 2D by systematically changing numerical resolutions and initial seed perturbations in multi-D radiation-hydrodynamic simulations. For the multi-group neutrino transport, the isotropic diffusion source approximation (IDSA) scheme (Liebendörfer et al. 2009) is implemented in a ray-by-ray manner (e.g., Takiwaki et al. (2012) for more details), which we have updated to achieve a very high computational efficiency. As in Takiwaki et al. (2012), we here focus on the evolution of an $11.2M_{\odot}$ star of Woosley et al. (2002). We choose this lighter progenitor because the shock revival occurs relatively earlier after bounce (e.g., Buras et al. (2006)) compared to more massive progenitor models as employed in Hanke et al. (2013). The updated transport scheme together with the employed earlier-to-explode progenitor allow us to conduct a systematic numerical study, for the first time, in both 2D and 3D (to the best of our knowledge) in the context of self-consistent neutrino-driven supernova models.

2. NUMERICAL METHODS AND MODELS

Here we briefly summarize several major updates of the code that we have implemented after our previous work (Takiwaki et al. 2012) in which the spectral neutrino transport scheme IDSA (Liebendörfer et al. 2009) was implemented in the ZEUS-MP code (Hayes et al. 2006).

In the original IDSA scheme, a steady-state approximation ($\partial f^s / \partial t = 0$) is assumed. Here f^s represents the *streaming* part of the neutrino distribution function (e.g., Liebendörfer et al. (2009)). Then one should deal with a Poisson-type equation to find the solution of f^s (e.g., Eq.(10) in Liebendörfer et al. (2009)). This is computationally expensive, because a collective data-communication is required on the MPI routines for all the processors (along the given radial direction in the ray-by-ray approximation) to solve the Cauchy problem.

To get around the problem, one needs to solve the evolution of f^s as,

$$\frac{\partial \mathcal{E}^s}{\partial t} + \frac{1}{r^2} \frac{\partial}{\partial r} r^2 \mathcal{F}^s = \mathcal{S}[j, \chi, \Sigma], \quad (1)$$

$$\mathcal{E}^s \equiv \frac{1}{2} \int d\mu f^s, \quad (2)$$

$$\mathcal{F}^s \equiv \frac{1}{2} \int \mu d\mu f^s, \quad (3)$$

$$\mathcal{S} \equiv -(\hat{j} + \hat{\chi}) \mathcal{E}^s + \Sigma, \quad (4)$$

where \mathcal{E}^s and \mathcal{F}^s corresponds to the radiation energy and flux of the streaming particle, and \mathcal{S} represents the source term that is a functional of the neutrino emissivity (j), absorptivity (χ), and the isotropic diffusion term (Σ) all defined in the laboratory frame, respectively. From local hydrodynamic quantities (density, Y_e , entropy), the source term of Eq.(1) ($\mathcal{S}[j, \chi, \Sigma]$) can

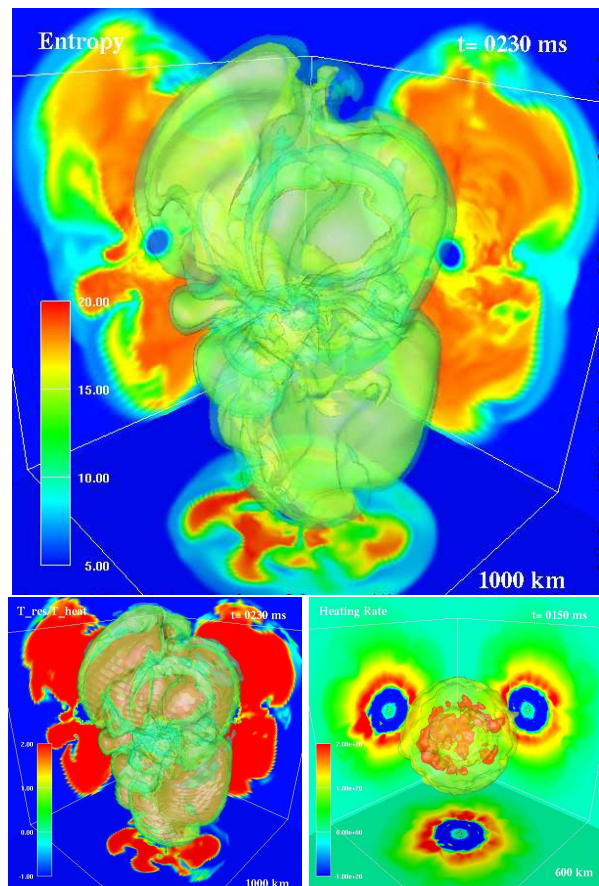


FIG. 1.— Three dimensional plots of entropy per baryon (top panel), $\tau_{\text{res}}/\tau_{\text{heat}}$ (bottom left panel) that is the ratio of the residency to the neutrino heating timescale (see the text for details), and the net neutrino heating rate (bottom right panel, in unit of $\text{erg cm}^{-3} \text{s}^{-1}$) for three snapshots (top and bottom left: $t = 230$ ms, and bottom right: $t = 150$ ms measured after bounce ($t \equiv 0$) of our model 3D-H-1). The contours on the cross sections in the $x = 0$ (back right), $y = 0$ (back bottom), and $z = 0$ (back left) planes are, respectively, projected on the sidewalls of the graphs. For each snapshot, the length of white line is indicated at right bottom text.

be determined. For closure, we use a prescribed relation between the radiation energy and flux as ($\mathcal{F}^s/\mathcal{E}^s = \frac{1}{2}(1 + \sqrt{1 - [R_\nu/\max(r, R_\nu)]^2})$ with R_ν being the radius of an energy-dependent scattering sphere (see Eq.(11) in Liebendörfer et al. (2009)). Since the cell-centered value of the flux, \mathcal{F}^s , is obtained by the prescribed relation, the cell-interface value is estimated by the first-order upwind scheme assuming that the flux is out-going along the radial direction. With the numerical flux, the transport equation of \mathcal{E}^s (Eq.(1)) now expressed in a hyperbolic form is numerically solved. This modification does not produce any significant changes in the numerical results (see Takiwaki et al. in preparation for more details), however, the computational cost becomes more than 10 times smaller than that in the previous treatment. The velocity dependent terms ($O(v/c)$) are only included (up to the leading order) in the trapped part of the distribution function (Eq. (15) in Liebendörfer et al. (2009)). Concerning heavy-lepton neutrinos ($\nu_x = \nu_\mu, \nu_\tau, \bar{\nu}_\mu, \bar{\nu}_\tau$), we employ a leakage scheme to include the ν_x cooling via pair-, photo-, plasma processes (e.g., Rosswog & Liebendörfer (2003);

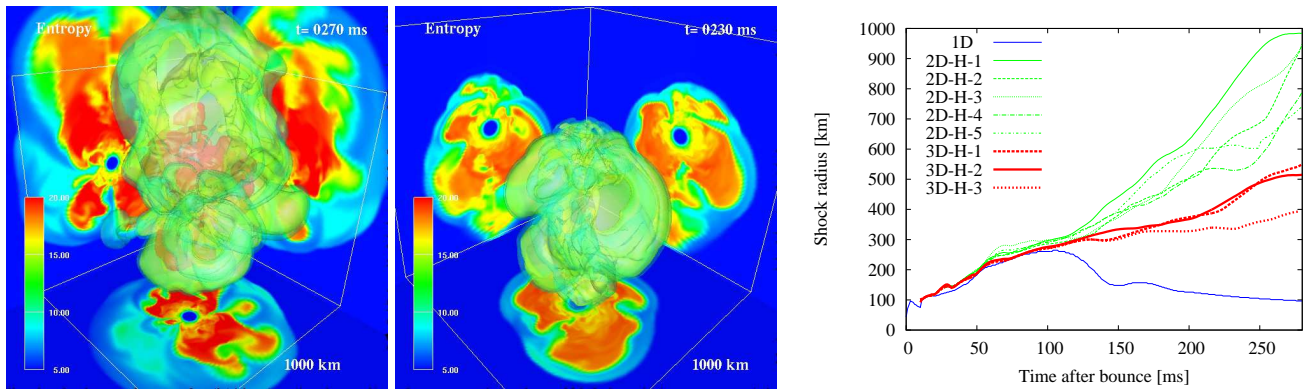


FIG. 2.— Same as the top panel in Figure 1 but for models 3D-H-2 (left panel) and 3D-H-3 (middle panel), which produces stronger explosions closely toward the north (left panel) and south pole (middle panel), respectively. Right panel shows the evolution of average shock radii for the high-resolution 2D (green lines) and 3D (red lines) models explored in this study (e.g., Table 1).

Itoh et al. (1989)). We apply the so-called ray-by-ray approach in which the neutrino transport is solved along a given radial direction assuming that the hydrodynamic medium for the direction is spherically symmetric. To improve the accuracy of total energy conservation, we follow the prescription proposed by Müller et al. (2010). For the calculations presented here, self-gravity is computed by a Newtonian monopole approximation. We use the equation of state (EOS) by Lattimer & Swesty (1991) with a compressibility modulus of $K = 180$ MeV (LS180).

Our fiducial 3D models are computed on a spherical polar grid with a resolution of $n_r \times n_\theta \times n_\phi = 320 \times 64 \times 128$, in which non-equally spaced radial zones covers from the center to an outer boundary of 5000 km. The radial grid is chosen such that the resolution Δr is better than 2 km in the PNS interior and typically better than 5 km outside the PNS. For the spectral transport, we use 20 logarithmically spaced energy bins ranging from 3 to 300 MeV and we take a ray-by-ray approximation (e.g., Buras et al. (2006); Bruenn et al. (2013)), in which a ray is cast for every angular zone. In all the multi-D runs, the innermost 5 km is computed in spherical symmetry to avoid excessive time-step limitations. Seed perturbations for aspherical instabilities are imposed by hand at 10 ms after bounce by introducing random perturbations of 1% in velocity behind the stalled shock.

To test the sensitivity of the supernova dynamics to numerical resolutions, we compute 3D model-series with lower angular resolutions, namely half or quarter of the (equidistant) mesh numbers in the azimuthal direction ($n_r \times n_\theta \times n_\phi = 320 \times 64 \times 64$ and $n_r \times n_\theta \times n_\phi = 320 \times 64 \times 32$). In 2D simulations we vary the mesh numbers in the lateral direction as $n_r \times n_\theta = 320 \times 64$, $n_r \times n_\theta = 320 \times 128$ and $n_r \times n_\theta = 320 \times 256$, respectively (see Table 1). In the table, model 3D-H-1 differs from model 3D-H-2 (and 3D-H-3 etc) only in the random seed perturbations (with the perturbation amplitudes being the same in all cases). Note that the lowest-resolution 3D model in this work corresponds to the best-resolution model in Takiwaki et al. (2012). By using the fastest K computer in Japan, it took typically 1.3 months (equivalently ~ 4 million core-hour computing-time) for each of our 3D fiducial models.

3. RESULT

As summarized in Table 1, all the computed models including nine 3D models and fifteen 2D models exhibit shock revival, leading to the possibility of explosion. Before going into detail how the explosion dynamics and stochasticity are different in 2D and 3D, we briefly outline the hydrodynamics features taking model 3D-H-1 as an example.

The top panel of Figure 1 shows the blast morphology of model 3D-H-1 at $t_{\text{pb}} = 230$ ms (postbounce) when the revived shock is reaching an angle-averaged radius of 400 km (e.g., red dashed line in the right panel of Figure. 2). As seen from the side wall panels, a bipolar explosion is obtained for this model. The bottom left panel (red regions) shows that the ratio of the residency timescale to the neutrino heating timescale (e.g., Equations (6) and (7) in Takiwaki et al. (2012)) exceeds unity behind the shock, which presents evidence that the shock revival is driven by the neutrino-heating mechanism. The bottom right panel of Figure 1 depicts spatial distribution of the net neutrino heating rate at $t_{\text{pb}} = 150$ ms. Small scale inhomogeneities (colored as red or yellow) are seen, which predominantly comes from neutrino-driven convection and anisotropies of the accretion flow, but the shape of the gain region is very close to be spherical before the onset of an explosion. This suggests that the bipolar geometry of the shock is produced not by the global anisotropy of the neutrino sphere, but by multi-D effects such as by neutrino-driven convection and the SASI in the gain regions after the explosion (gradually) sets in.

Reflecting the stochastic nature of the multi-D neutrino-driven explosions, the blast morphology changes from models to models. The left and middle panels of Figure 2 show that a stronger explosion is obtained toward the north direction (model 3D-H-2) and the south pole (model 3D-H-3), which is only different from model 3D-H-1 (e.g., Table 1) in terms of the imposed initial random perturbations. Note that due to the use of the spherical coordinates, we cannot omit the possibility that the polar axis still gives a special direction in our 3D simulations. But more importantly, our results show that the final fate of the 3D and 2D models whether an explosion is obtained or not, is little affected by the stochasticity of the explosion geometry.

In fact, the right panel of Figure 2 shows the evolution of the average shock radius for our 1D (blue line), 2D (green lines), and 3D (red lines) models, respectively.

TABLE 1
 MODEL SUMMARY

Model	$n_r \times n_\theta \times n_\phi$	Angular resolution [°]	t_{400} [ms]	$t_{400,av}$ [ms]	$\sigma[t_{400}]$ [ms]	t_{end} [ms]	R_{max} [km]	E_{diag} [10^{50} erg]	$(\ell, m)_{max}$	$ c_{\ell, m} _{max}$
3D-H-1	$320 \times 64 \times 128$	$2.8^\circ \times 2.8^\circ$	223			284	550	0.15	1,0	0.02
3D-H-2	$320 \times 64 \times 128$	$2.8^\circ \times 2.8^\circ$	216	236	24	369	850	0.25	2,0	0.02
3D-H-3	$320 \times 64 \times 128$	$2.8^\circ \times 2.8^\circ$	269			269	400	0.15	2,0	0.02
3D-M-1	$320 \times 64 \times 64$	$2.8^\circ \times 5.6^\circ$	192			269	600	0.25	1,0	0.01
3D-M-2	$320 \times 64 \times 64$	$2.8^\circ \times 5.6^\circ$	194	194	1.2	319	700	0.30	1,0	0.02
3D-M-3	$320 \times 64 \times 64$	$2.8^\circ \times 5.6^\circ$	195			279	700	0.27	1,0	0.01
3D-L-1	$320 \times 64 \times 32$	$2.8^\circ \times 11.3^\circ$	193			314	1000	0.60	2,1	0.009
3D-L-2	$320 \times 64 \times 32$	$2.8^\circ \times 11.3^\circ$	188	188	4	273	800	0.45	2,1	0.009
3D-L-3	$320 \times 64 \times 32$	$2.8^\circ \times 11.3^\circ$	183			273	700	0.35	2,1	0.01
2D-H-1	320×256	0.7°	138			300	1100	0.65	1,0	0.05
2D-H-2	320×256	0.7°	154			329	1200	0.45	2,0	0.08
2D-H-3	320×256	0.7°	159	151	7	311	1200	0.76	2,0	0.1
2D-H-4	320×256	0.7°	156			368	1500	0.6	2,0	0.05
2D-H-5	320×256	0.7°	150			345	1200	0.7	2,0	0.1
2D-M-1	320×128	1.4°	140			369	1700	0.5	1,0	0.1
2D-M-2	320×128	1.4°	125			319	1800	0.8	2,0	0.06
2D-M-3	320×128	1.4°	151	142	10	400	1700	0.85	1,0	0.1
2D-M-4	320×128	1.4°	144			469	2300	1.0	1,0	0.1
2D-M-5	320×128	1.4°	152			400	1800	1.0	2,0	0.05
2D-L-1	320×64	2.8°	137			387	2100	1.1	2,0	0.08
2D-L-2	320×64	2.8°	137			395	2200	1.26	2,0	0.1
2D-L-3	320×64	2.8°	126	133	6	483	2800	1.3	1,0	0.09
2D-L-4	320×64	2.8°	140			559	2400	1.3	1,0	0.09
2D-L-5	320×64	2.8°	125			569	2500	1.3	2,0	0.05

Note that ‘‘H’’, ‘‘M’’, or ‘‘L’’ appended to our models stands for high, moderate, low azimuthal angular resolutions, respectively. The third number ($-i$) of each model that runs from 1 to 3 for 3D models and from 1 to 5 for 2D models represents the difference only in the random seed perturbations (with the perturbation amplitudes being the same in all cases). t_{400} represents the time when the average shock radius touches a radius of 400 km, and $t_{400,av}$ and $\sigma[t_{400}]$ denotes the model average and the dispersion of t_{400} . t_{end} denotes the time of the end of the simulation. R_{max} and E_{diag} are the averaged shock radius and the diagnostic explosion energy at t_{end} . $(\ell, m)_{max}$ denotes the set of spherical harmonics mode when the normalized amplitude takes the maximum value ($|c_{\ell, m}|_{max}$) during the linear SASI phase.

Before the onset of shock revival (before 100 ms after bounce), the evolution of the shock is all similar to that of the 1D model (blue line). After that, our results show that the shock expansion is systematically more energetic in 2D (green lines) than in 3D (red lines). This feature is qualitatively consistent with Takiwaki et al. (2012), and also with Hanke et al. (2013) who recently reported 2D vs. 3D comparison based on a single 3D model but employing more detailed neutrino transport than ours.

Due to our lack of necessary computational resources, our 3D models should be terminated typically before $t_{end} \lesssim 300$ ms postbounce (e.g., in Table 1), but we expect them to produce explosions subsequently, seeing a continuous shock expansion out to a radius of 500 km in 3D (and 700 km in 2D). Given the same numerical resolution (e.g., model series 3D-L in Table 1), the average shock radii in this study is smaller than those in Takiwaki et al. (2012), in which the cooling by heavy-lepton neutrinos was not taken into account. Due to the inclusion of the ν_x cooling, the (angle-averaged) $\bar{\nu}_e$ luminosity decreases more quickly after bounce (compare Figure 3 and Figure 14 of Takiwaki et al. (2012)), which leads to the less energetic shock expansion in this study. It should be mentioned that by comparing our ν_x luminosity estimated by the leakage scheme with that obtained by the work by Buras et al. (2006) with detailed neutrino transport, the peak luminosity is more than 20 % smaller in our case. Such underestimation of cooling by heavy-lepton neutrinos should lead to artificially

larger maximum shock extent ($R_{max} \sim 260$ km, blue line in the right panel of Figure 2) compared to $R_{max} \sim 170$ km in Buras et al. (2006). We have to emphasize that the use of the leakage scheme together with the omission of inelastic neutrino scattering on electrons and GR effects in the present scheme is likely to facilitate artificially easier explosions. Regarding our 2D models, the relatively earlier shock revival (~ 100 ms postbounce) coincides with the decline of the mass accretion rate onto the central PNS. This could be the reason that the timescale is similar to that in Müller et al. (2012) who reported 2D (GR) models for the same progenitor model with detailed neutrino transport.

As seen from Figure 3, the angle average neutrino luminosity ($\langle L_\nu \rangle$) and the mean neutrino energy ($\langle \epsilon_\nu \rangle = \int E^3 \mathcal{F}^s dE / \int E^2 \mathcal{F}^s dE$, where E is neutrino energy) is barely affected by the imposed initial perturbations (presumably at few-percent levels in amplitudes). This again supports our finding that the explosion stochasticity is very influential to determine the blast morphology but not the working of the neutrino-heating mechanism.

From the bottom panel of Figure 3, it can be seen that overall trend in the neutrino luminosities and the mean energies is similar between our 3D and 2D model. The neutrino luminosities in the 2D model (green lines) show a short-time variability (with periods of milliseconds to $\gtrsim 10$ ms) after around 100 ms postbounce. Such fast variations in the postbounce luminosity evolution

have been already found in previous 2D studies (e.g., Ott et al. (2008); Marek et al. (2009)). This is caused by the modulation of the mass accretion rate due to convective plumes and downflows hitting onto the PNS surface (see also Lund et al. (2012); Tamborra et al. (2013) about the detectability of these neutrino signals). It is interesting to note that such fast variability is less pronounced in our 3D model (red lines in the bottom panel). This is qualitatively consistent with Lund et al. (2012) who analyzed the neutrino signals from 2D and 3D models, in which an approximate neutrino transport was solved (Wongwathanarat et al. 2010) as in Scheck et al. (2006).

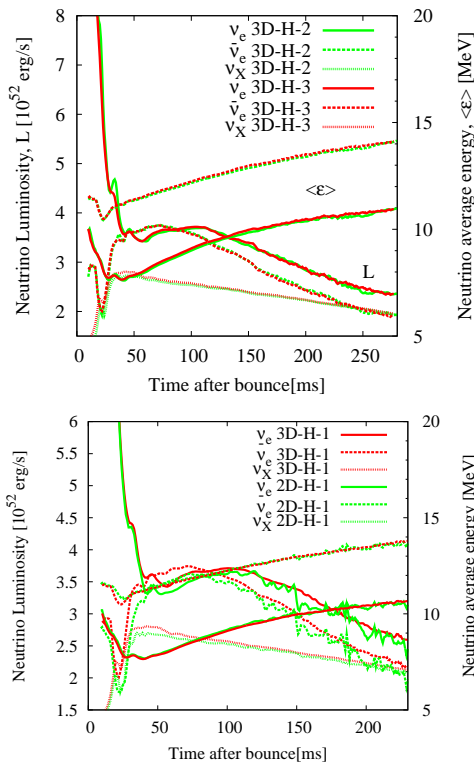


FIG. 3.— Top panel shows time evolution of neutrino luminosities and mean energies of electron (ν_e), anti-electron ($\bar{\nu}_e$), or heavy-lepton (ν_X) neutrinos for models 3D-H-2 (green line) and 3D-H-3 (red line), respectively. Bottom panel is the same as the top panel but for the comparison between 2D and 3D (for models 3D-H-1 and 2D-H-1). These quantities are estimated at 500 km.

Figure 4 shows evolution of the average PNS radius for the 1D (blue line), 2D (green line), and 3D models (red line), respectively, that are defined by a fiducial density of $10^{11} \text{ g cm}^{-3}$. The PNS contraction is similar among the 1D, 2D, and 3D models. Although the PNS contraction potentially affect the evolution of the shock (Hanke et al. 2013; Suwa et al. 2013), in our cases that are unchanged by the difference of the dimension and that are not main agent to explain the divergence of the shock evolution in 1D, 2D and 3D. The PNS contraction is slightly stronger in the later postbounce phase in 1D ($\gtrsim 150$ ms postbounce, compare blue with green and red lines) compared to 2D and 3D because no shock revival was obtained in the 1D model and heavier PNS and slightly deeper gravitational potential are obtained compared to that of the multi-D models. In the figure, three

more lines (solid, dashed, dotted gray lines) are plotted, in which we estimate the evolution of the PNS radius based on the fitting formula (equation (1) of Scheck et al. (2006)) by changing a final radius of PNS R_f for a given set of an exponential timescale of $t_{\text{ib}} = 1$ s and an initial radius of PNS $R_i = 85$ km. As can be seen, the dashed gray line ($R_f = 12$ km) can most closely reproduce our results, which is just between the slow and fast contraction investigated in the work by Hanke et al. (2013).

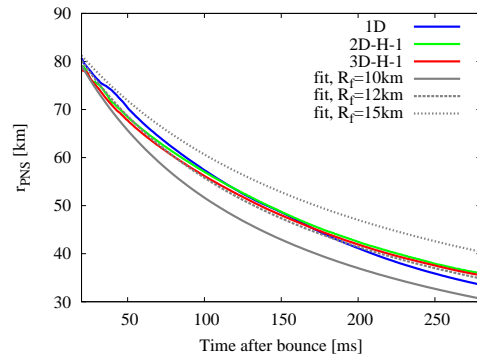


FIG. 4.— Average PNS radius (defined by a fiducial density of $10^{11} \text{ g cm}^{-3}$) for the 1D (blue line), 2D (green line), and 3D models (red line), respectively. The gray lines labeled as "fit" corresponds to the prescribed PNS evolution with three different values of $R_f = 10, 12,$ and 15 km (see text for more details).

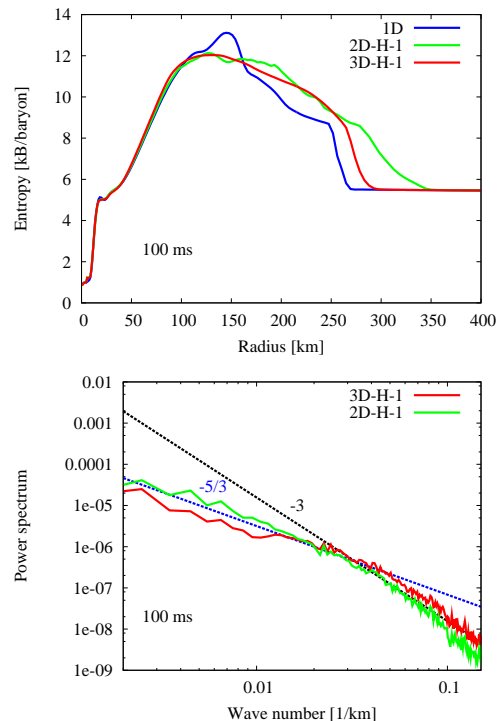


FIG. 5.— Top panel shows radial profiles of angle-averaged entropy at 100 ms postbounce for the 1D, 2D-H-1, 3D-H-1 model, respectively. Bottom panel shows spectra of the turbulent kinetic energy as a function of wavenumber (k) between our 2D (green line) and 3D (red line) model, respectively.

Top panel of Figure 5 shows angle-averaged entropy profile at 100 ms postbounce, after when the difference of the subsequent shock evolution between our

1D, 2D, and 3D models becomes remarkable (e.g., right panel in Figure 2). As has been studied in detail since 1990's (e.g., Herant et al. (1994); Burrows et al. (1995); Janka & Müller (1996)), buoyancy-driven convection supported by turbulence (e.g., Murphy et al. (2013)) transports heat radially outward, leading to a more extended entropy profile in the 2D (green line in the panel) and 3D (red line) model compared to the 1D model (blue line) (see also Hanke et al. (2012)).

Bottom panel of Figure 5 compares the turbulent energy spectra of the anisotropic velocity (Takiwaki et al. (2012)) as a function of wavenumber (k) between our 2D (green line) and 3D (red line) model, respectively. The green and red line crosses at around $k_{\text{cross}} = 0.02/\text{km}$ (corresponding to ~ 50 km in spacial scale), above which the amplitude for the 3D model (red line) dominates over that for the 2D model (green), below which the amplitude for the 2D model does for the 3D model. This is qualitatively consistent with the previous results using the light-bulb method (e.g., Hanke et al. (2012); Burrows et al. (2012); Dolence et al. (2013); Couch (2013); Fernández et al. (2013)). By comparing the 2D and 3D curve with spectral slopes labeled by the corresponding exponent ($-5/3$:dotted blue line, -3 :dotted black line), the power-low dependence ($\propto k^{-5/3}$) approximately holds for $k_{\text{int}} \lesssim 0.02/\text{km}$ in the 2D model (green line) presumably as a result of the inverse energy cascade (Kraichnan 1967). Above k_{cross} , the slope of the 3D model (red line) become more closer to $k^{-5/3}$ (blue line), while the spectrum slope of the 2D model drops much steeply with the wave number as k^{-3} (gray line). These features are again in accord with the previous studies mentioned above (e.g., Hanke et al. (2012); Burrows et al. (2012); Dolence et al. (2013); Couch (2013); Fernández et al. (2013)).

As shown in the middle panel of Figure 2, model 3D-H-3 produces one-sided explosion towards the south pole during the simulation time. Reflecting the unipolarity, the average shock radius is smaller than for the other 3D models (compare dotted line (in red) with solid and dashed red (in red) in the right panel of Figure 2). To quantify the vigor of the shock expansion, t_{400} is a useful quantity that was defined in Hanke et al. (2012) as the moment of time when the shock reaches an average radius of 400 km. In fact, as seen from Table 1, t_{400} of model 3D-H-3 ($t_{400} \approx 270$ ms) is delayed about 50 ms compared to those of models 3D-H-1 and 3D-H-2 ($t_{400} \approx 220$ ms).

The model average of t_{400} (e.g., $t_{400,\text{av}}$ in Table 1) clearly shows that models with higher numerical resolutions lead to slower onset of the shock revival in both our 3D and 2D models. This feature is qualitatively consistent with the 2D self-consistent models by Marek & Janka (2009) and with the 3D idealized models by Hanke et al. (2013); Couch (2013), respectively.

σ_{400} in Table 1 represents the model dispersion of t_{400} , which varies much more stochastically in 3D models with different numerical resolution (from 1.2 to 24 ms) than those in 2D (from 6 to 10 ms). For model 3D-H-3, the shock revival is most delayed (e.g., Table 1) and the shock expansion is weakest among the computed models (dotted red line in Figure 1). Nagakura et al. (2013) proposed that shock revival is very sensitive to the imposed seed perturbations near the stalled shock. Following the

hypothesis, we speculate that the influence of seed perturbations is seen most remarkably in our weakest explosion model.

E_{diag} in Table 1 denotes the diagnostic energy defined as the total energy (internal plus kinetic plus gravitational), integrated over all matter where the sum of the corresponding specific energies is positive. We include recombination energy in internal energy (Bruenn et al. (2013)). Reflecting the earlier shock revival, the diagnostic energy is systematically bigger in 2D than in 3D. These diagnostic energies when we terminated the simulation were typically on the order of $\sim 10^{49}$ erg and $\sim 10^{50}$ erg for our 3D and 2D models, respectively. It should be noted that this quantity is estimated at the end of simulation, t_{end} . In order to compare the *diagnostic* energy with the observed kinetic explosion energy ($\sim 10^{51}$ erg), a much longer-term simulation including improved microphysics, general relativity, and nuclear burning would be needed.

Recently it is enthusiastically discussed which one between neutrino-driven convection and the SASI plays a more crucial role in facilitating neutrino-driven explosions (Foglizzo et al. 2006; Dolence et al. 2013; Murphy et al. 2013; Burrows et al. 2012; Hanke et al. 2012, 2013). The left panel of Figure 6 shows the time evolution of the Foglizzo parameter χ (Foglizzo et al. 2006) As seen, χ continuously exceeds the critical number of 3 (Foglizzo et al. 2006) rather shortly after bounce (~ 40 ms), marking the transition to the non-linear phase. The earlier onset of the shock revival and the absence of clear features of the SASI in the linear phase (see discussion below) could indicate that neutrino-driven convection dominates over the SASI when the explosion sets in (e.g., at t_{400} in Table 1).

The right panel of Figure 6 shows the evolution of normalized coefficient of spherical harmonics of the shock surface for model 3D-H-1. No clear feature of the linear growth of the SASI ($\lesssim 40$ ms postbounce) was obtained for the $11.2 M_{\odot}$ star explored in this work. In both our 3D and 2D models, the qualitative behaviors of the harmonic modes seen in Figure 6 are less sensitive to the employed numerical resolution and seed random perturbations (see appendix A). The dominant channels are of low modes (e.g., $(\ell, m)_{\text{max}}$ in Table 1), the amplitudes of which (e.g., $|c_{\ell, m}|_{\text{max}}$ in the table) are systematically larger in 2D than in 3D. This is qualitatively consistent with previous 3D simulations employing different numerical setups (e.g., Nordhaus et al. (2010); Hanke et al. (2012); Burrows et al. (2012); Hanke et al. (2013)).

After the linear phase comes to an end at around 100 ms postbounce, the trajectory of the revived shock shows a wider diversity (e.g., Figure 1) depending on the employed numerical resolution and seed perturbations.

4. SUMMARY AND DISCUSSION

Studying an $11.2 M_{\odot}$ and changing numerical resolutions and seed perturbations systematically in the multi-D simulations employing the updated IDSA scheme, we studied how the postbounce dynamics is different in 2D and 3D. All the computed models exhibit the neutrino-driven revival of the stalled bounce shock, leading to the possibility of an explosion. Though the blast morphology changes from models to models reflecting the stochastic nature of multi-D neutrino-driven explosions,

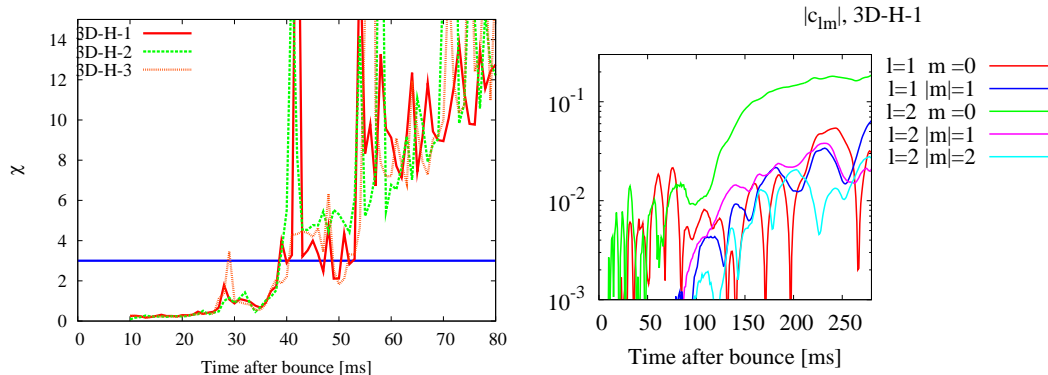


FIG. 6.— Time evolution of χ parameter (left panel) and normalized spherical harmonic mode amplitudes of the shock for our 3D high-resolution models with respect to each (ℓ, m) (right panel, e.g., $|c_{\ell m}/c_{00}|$ in equation (10) of Takiwaki et al. (2012)). The horizontal blue line corresponds to $\chi = 3$, above which neutrino-driven convection dominates over the SASI (Foglizzo et al. 2006). In the right panel, lower modes with larger amplitudes are selected.

it was found that the final fate of these multi-D models whether an explosion is obtained or not, is little affected by the explosion stochasticity at least in the current investigated progenitor model. In line with some previous studies, higher numerical resolutions lead to slower onset of the shock revival in both 3D and 2D. Our results systematically showed that the revived shock expands more energetically in 2D than in 3D.

The caveats of our 3D models include the ray-by-ray approximation, the use of the softer EOS, and the omission of detailed neutrino reactions and general relativity (e.g., Kuroda et al. (2012); Ott et al. (2013)). Keeping our efforts to improve them, it is important to study the dependence of progenitors (e.g., Buras et al. (2006); Bruenn et al. (2013)) and EOS (e.g., Marek & Janka (2009); Suwa et al. (2013)) on the neutrino-driven mechanism in 3D computations. A number of exciting issues also remain to be investigated, such as gravitational-wave signatures (e.g., Kotake (2013)), neutrino emission and

its detectability (e.g., Lund et al. (2012)), and the possibility of 3D SASI flows generating pulsar kicks and spins (e.g., Wongwathanarat et al. (2013)). Shifting from individuals to populations of 3D models, a rush of 3D explorations with increasing sophistication is now going to shed light on these fascinating riddles (hopefully not in the distant future) with increasing supercomputing resources on our side.

We are thankful to K. Sato and S. Yamada for continuing encouragements. Numerical computations were carried on in part on the K computer at the RIKEN Advanced Institute for Computational Science (Proposal number hp120285), XC30/XT4 at NAOJ, and on SR16000 at YITP in Kyoto University. This study was supported in part by Grants-in-Aid for Scientific Research (Nos. 23540323, 23340069, 24244036, and 25103511) and by HPCI Strategic Program of Japanese MEXT.

APPENDIX

DEPENDENCE ON THE AMPLITUDE OF SEED PERTURBATIONS

In this Appendix we briefly report on the dependence on the amplitudes of the initial seed perturbations. We have added a radial velocity perturbation, $\delta v_r(r, \theta, \phi)$ to the profile obtained by 1D simulation, $v_r^{1D}(r)$, according to the equation $\delta v_r = p_{\text{amp}} \text{rand} \times v_r^{1D}$ where rand is pseudorandom number that takes the value from -1 to 1 and p_{amp} represents the absolute amplitude of the seed perturbations that we take as 1% in the models discussed in the main section. Let us firstly note that the amplitude of seed perturbations $a_{\ell, m}$ assumed in this study scales as $p_{\text{amp}}/N^{1/2}$, where $a_{\ell, m}$ denotes the amplitude of the (ℓ, m) component of the seed perturbations at a given radius (i.e. $a_{\ell, m} = \int d\phi \int \sin\theta d\theta (v_r^{1D} + \delta v_r) Y_{\ell, m}^*$, where $Y_{\ell, m}^*$ is conjugate of spherical harmonic function) and $N = n_\theta \times n_\phi$ represents the total angular mesh number where n_θ, n_ϕ being the mesh number in the θ and ϕ direction, respectively (e.g. in our 3D model with highest resolution, $n_\theta = 64, n_\phi = 128$). Therefore the seed amplitudes assumed in this work depend on numerical resolution (i.e., N).

If we keep the seed amplitudes ($a_{\ell, m}$) constant for models with different resolutions, will our results change drastically? Since we cannot rerun 3D models due to the limited computational resources, we compute a number of 2D models to answer to this question. First of all, let us discuss 2D models with different seed amplitudes. Top panel of Figure 7 shows the evolution of $c_{1,0}$ (the normalized harmonic amplitudes of shock position) for 2D models with $p_{\text{amp}} = 1\%$ (red lines) or $0.176\% (= 1\%/\sqrt{32})$ (green lines) with five different realizations of initial random perturbation. The reduced amplitude is determined by the ratio of total grid number of 2D-H models and 3D-H models (i.e. $1/\sqrt{32} = \sqrt{n_{\theta|2D-H}/(n_\theta n_\phi)|_{3D-H}}$). One might have a guess that $c_{\ell, m}(t)$ could evolve as $a_{\ell, m} \exp(t/t_0)$ with t_0 representing the duration of the linear growth rate of hydrodynamic instabilities including the SASI or neutrino-driven convection. If this could be the case, the linear growth amplitude (at before 35 ms postbounce in the top panel) should be higher about $\sqrt{32}$ times for red lines compared to green lines. But as it is shown, this is not the case². And after

² Note that if the initial seed perturbations would be more bigger than those assumed in this study, they should affect the

postbounce hydrodynamics (see Couch & Ott (2013))

the early rising phase (about 40 ms postbounce in the panel), the saturation amplitudes are shown to be insensitive to the initial perturbation amplitudes (for the initial strength employed above). Remembering that neutrino-driven convection is likely to dominate over the SASI in the non-linear regime for the $11.2 M_{\odot}$ progenitor employed in this work, the delay of t_{400} (in the non-linear phase) for models with higher numerical resolutions cannot be also simply ascribed to the difference of the seed amplitudes.

Bottom panels of Figure 7 show evolution of $c_{1,0}$ for different resolution (H, M, and L) for our 2D and 3D models, respectively. For a given numerical resolution, t_{400} of the chosen models in these plots is close to a median of t_{400} for each model series. Note that in these models the initial seed amplitudes are dependent on both resolution and dimension. As can be seen, in both 2D and 3D, the amplitudes in the linear phase (< 40 ms postbounce) are comparable for models with different resolutions. And in the non-linear regime, no monotonic dependence of the non-linear evolution on the initial seed amplitudes (between H, M, L models) can be found. These results show that the findings in this work are less sensitive to the assumed initial seed perturbations.

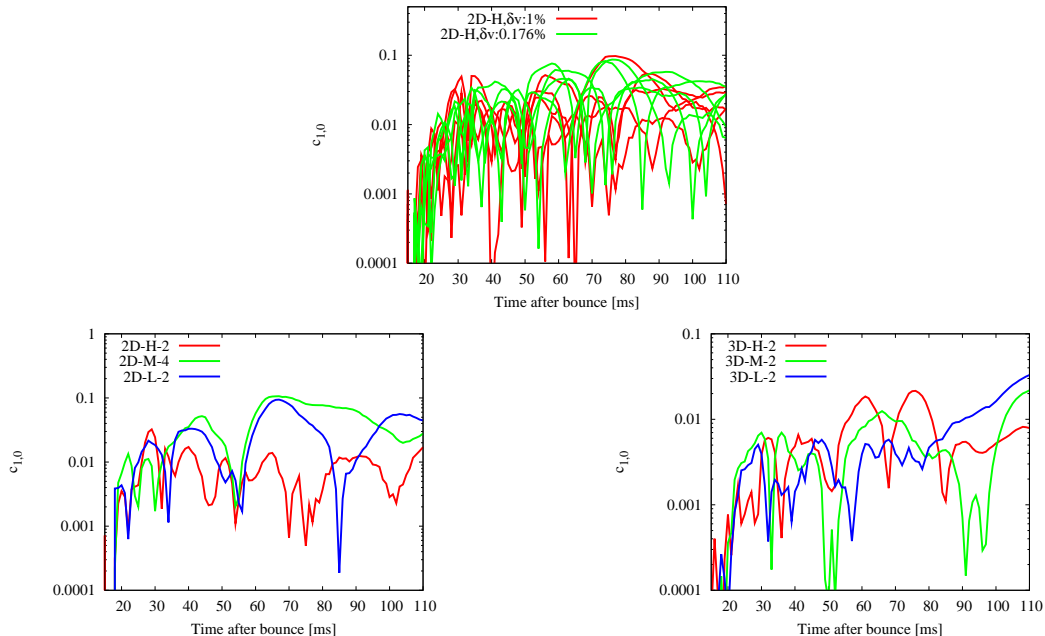


FIG. 7.— Top panel shows evolution of $c_{1,0}$ for our 2D models with $p_{\text{amp}} = 1\%$ (red lines) or 0.176% ($= 1\%/\sqrt{32}$) (green lines) with 5 different realizations of random perturbation (see text for more details). Bottom panels show evolution of $c_{1,0}$ for different resolution (H, M, and L) for our 2D and 3D models.

REFERENCES

- Bethe, H. A., & Wilson, J. R. 1985, *ApJ*, 295, 14
 Blondin, J. M., Mezzacappa, A., & DeMarino, C. 2003, *Astrophys. J.*, 584, 971
 Bruenn, S. W., Mezzacappa, A., Hix, W. R., et al. 2013, *ApJ*, 767, L6
 Buras, R., Janka, H.-T., Rampp, M., & Kifonidis, K. 2006, *A&A*, 457, 281
 Burrows, A., Hayes, J., & Fryxell, B. A. 1995, *ApJ*, 450, 830
 Burrows, A. 2013, *Reviews of Modern Physics*, 85, 245
 Burrows, A., Dolence, J. C., & Murphy, J. W. 2012, *ApJ*, 759, 5
 Burrows, A., Hayes, J., & Fryxell, B. A. 1995, *ApJ*, 450, 830
 Colgate, S. A., & White, R. H. 1966, *ApJ*, 143, 626
 Couch, S. M. 2013, *ApJ*, 775, 35
 Couch, S. M., & Ott, C. D. 2013, *ApJ*, 778, L7
 Demorest, P. B., Pennucci, T., Ransom, S. M., Roberts, M. S. E., & Hessels, J. W. T. 2010, *Nature*, 467, 1081
 Dolence, J. C., Burrows, A., Murphy, J. W., & Nordhaus, J. 2013, *ApJ*, 765, 110
 Endeve, E., Cardall, C. Y., Budiardja, R. D., & Mezzacappa, A. 2010, *ApJ*, 713, 1219
 Endeve, E., Cardall, C. Y., Budiardja, R. D., et al. 2012, *ApJ*, 751, 26
 Fernández, R. & Thompson, C. 2009a, *ApJ*, 703, 1464
 —. 2009b, *ApJ*, 697, 1827
 Fernández, R. 2010, *ApJ*, 725, 1563
 Fernández, R., Mueller, B., Fogliizzo, T., & Janka, H.-T. 2013, arXiv:1310.0469
 Fogliizzo, T., Scheck, L. & Janka, H.-Th., 2006, *ApJ*, 652, 1436
 Fogliizzo, T., Galletti, P., Scheck, L., & Janka, H.-T. 2007, *ApJ*, 654, 1006
 Fogliizzo, T., Masset, F., Guilet, J., & Durand, G. 2012, *Physical Review Letters*, 108, 051103
 Furusawa, S., Nagakura, H., Sumiyoshi, K., & Yamada, S. 2013, *ApJ*, 774, 78
 Fryer, C. L., Holz, D. E., & Hughes, S. A. 2002, *Astrophys. J.*, 565, 430
 Hanke, F., Marek, A., Müller, B., & Janka, H.-T. 2012, *ApJ*, 755, 138
 Hanke, F., Müller, B., Wongwathanarat, A., Marek, A., & Janka, H.-T. 2013, *ApJ*, 770, 66
 Hayes, J. C., Norman, M. L., Fiedler, R. A., Bordner, J. O., Li, P. S., Clark, S. E., ud-Doula, A., & Mac Low, M. 2006, *ApJS*, 165, 188
 Herant, M., Benz, W., Hix, W. R., Fryer, C. L., & Colgate, S. A. 1994, *ApJ*, 435, 339
 Itoh, N., Adachi, T., Nakagawa, M., Kohyama, Y., & Munakata, H. 1989, *Astrophys. J.*, 339, 354
 Iwakami, W., Kotake, K., Ohnishi, N., Yamada, S., & Sawada, K. 2008, *Astrophys. J.*, 678, 1207
 —. 2009, *Astrophys. J.*, 700, 232

- Iwakami, W., Nagakura, H., & Yamada, S. 2013, arXiv:1308.0829
- Janka, H., & Müller, E. 1996, *A&A*, 306, 167
- Janka, H.-T. 2012, *Annual Review of Nuclear and Particle Science*, 62, 407
- Herant, M., Benz, W., Hix, W. R., Fryer, C. L., & Colgate, S. A. 1994, *ApJ*, 435, 339
- Kotake, K. 2013, *Comptes Rendus Physique*, 14, 318
- Kotake, K., Takiwaki, T., Suwa, Y., et al. 2012, *Advances in Astronomy*, 2012
- Kuroda, T., Kotake, K., & Takiwaki, T. 2012, *ApJ*, 755, 11
- Kraichnan, R. H. 1967, *Physics of Fluids*, 10, 1417
- Langanke, K., Martínez-Pinedo, G., Müller, B., et al. 2008, *Physical Review Letters*, 100, 011101
- Lattimer, J. M., & Swesty, F. D. 1991, *Nuclear Physics A*, 535, 331
- Liebendörfer, M., Mezzacappa, A., & Thielemann, F. 2001, *Phys. Rev. D*, 63, 104003
- Liebendörfer, M., Whitehouse, S. C., & Fischer, T. 2009, *ApJ*, 698, 1174
- Lund, T., Wongwathanarat, A., Janka, H.-T., Müller, E., & Raffelt, G. 2012, *Phys. Rev. D*, 86, 105031
- Marek, A., & Janka, H.-T. 2009, *Astrophys. J.*, 694, 664
- Marek, A., Janka, H.-T., Müller, E. 2009, *A&A*, 496, 475
- Müller, B., Janka, H.-T., & Dimmelmeier, H. 2010, *ApJS*, 189, 104
- Müller, B., Janka, H.-T., & Heger, A. 2012, *ApJ*, 761, 72
- Müller, B., Janka, H.-T., & Marek, A. 2013, *ApJ*, 766, 43
- Murphy, J. W., & Burrows, A. 2008, *ApJ*, 688, 1159
- Murphy, J. W., Dolence, J. C., & Burrows, A. 2013, *ApJ*, 771, 52
- Nagakura, H., Yamamoto, Y., & Yamada, S. 2013, *ApJ*, 765, 123
- Nordhaus, J., Burrows, A., Almgren, A., & Bell, J. 2010, *ApJ*, 720, 694
- Ohnishi, N., Kotake, K. & Yamada, S., 2006, *ApJ*, 641, 1018
- . 2007, *ApJ*, 667, 375
- Ott, C. D., Burrows, A., Dessart, L., & Livne, E. 2008, *ApJ*, 685, 1069
- Ott, C. D., Abdikamalov, E., Mösta, P., et al. 2013, *ApJ*, 768, 115
- Rampp, M., & Janka, H.-T. 2000, *Astrophys. J. Lett.*, 539, L33
- Rosswog, S., & Liebendörfer, M. 2003, *MNRAS*, 342, 673
- Scheck, L., Plewa, T., Janka, H.-T., Kifonidis, K., & Müller, E., 2004, *Phys. Rev. Lett.*, 92, 011103
- Scheck, L., Kifonidis, K., Janka, H.-T., Müller, E. 2006, *A&A*, 457, 963
- Scheck, L., Janka, H., Foglizzo, T., & Kifonidis, K. 2008, *A&A*, 477, 931
- Sumiyoshi, K., Yamada, S., Suzuki, H., et al. 2005, *Astrophys. J.*, 629, 922
- Suwa, Y., Kotake, K., Takiwaki, T., et al. 2010, *PASJ*, 62, L49+
- Suwa, Y., Kotake, K., Takiwaki, T., Liebendörfer, M., & Sato, K. 2011, *ApJ*, 738, 165
- Suwa, Y., Takiwaki, T., Kotake, K., et al. 2013, *ApJ*, 764, 99
- Takiwaki, T., & Kotake, K. 2011, *ApJ*, 743, 30
- Takiwaki, T., Kotake, K., & Suwa, Y. 2012, *ApJ*, 749, 98
- Tamborra, I., Hanke, F., Müller, B., Janka, H.-T., & Raffelt, G. 2013, *Physical Review Letters*, 111, 121104
- Thompson, T. A., Burrows, A., & Pinto, P. A. 2003, *Astrophys. J.*, 592, 434
- Wang, L., & Wheeler, J. C. 2008, *ARA&A*, 46, 433
- Wongwathanarat, A., Janka, H.-T., Müller, E. 2010, *ApJ*, 725, L106
- Wongwathanarat, A., Janka, H.-T., & Müller, E. 2013, *A&A*, 552, A126
- Woosley, S. E., Heger, A., & Weaver, T. A. 2002, *Reviews of Modern Physics*, 74, 1015